

# Effect of Drying on the Fabrication of MgAl Layered Double Hydroxides

Luiz D. Silva Neto, Chayene G. Anchieta, José L. S. Duarte, Lucas Meili,\* and José T. Freire

Cite This: *ACS Omega* 2021, 6, 21819–21829

Read Online

ACCESS |



Metrics &amp; More

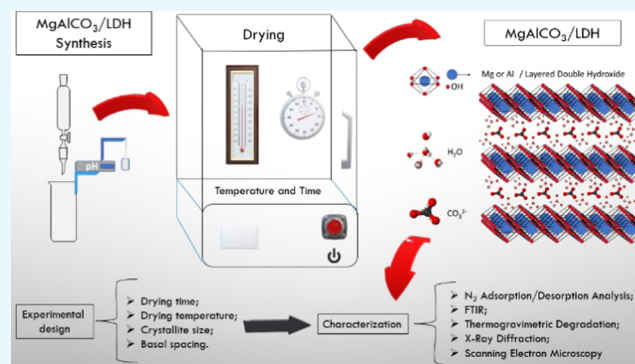


Article Recommendations



Supporting Information

**ABSTRACT:** This study aimed to evaluate the synthesis of MgAl/LDH from the drying process perspective, evaluating the influence of temperature (75–90 °C) and time (16–20 h) in the drying process. The synthesis was performed, maintaining a ratio of 2:1 of Mg/Al, and the drying was conducted according to a 2<sup>2</sup> experimental design: four axial points and three repetitions at the central point. The surface area and pore diameter ranged from 4.09 to 18.55 m<sup>2</sup>/g and 12.50 to 24.46 nm. Fourier transform infrared (FTIR) analysis indicated the drying-caused variation of the LDH typical bands intensities. Scanning electron microscopy (SEM) images showed the tendency of the increase of agglomeration with the temperature elevation. The drying parameters' influence was evident for X-ray diffraction (XRD) analysis observing the crystallite size increment, from 13.10 to 38.94 nm, and basal spacing variation, from 7.52 to 7.64 Å. The statistical models for growing crystal and reduction of the basal spacing were physically consistent but with low values of R<sup>2</sup>. The drying time and temperature had a considerable influence on the chemical, physical, structural, and morphological properties of LDH.



## 1. INTRODUCTION

Layered double hydroxides (LDHs), also known as anionic clays, have received considerable attention in recent years due to their specific structures with different potential applications. Due to its double hydroxide layers with interlamellar anions, LDHs have great structural, chemical, electronic, ionic, optical, and magnetic versatility that can be used in a powder form, granular form, dispersed in a solid, or in a liquid medium. LDHs are commonly represented by the general formula  $[M_{1-x}^{II}M_x^{III}(\text{OH})_2]^{x+} [A^{n-}]_x z\text{H}_2\text{O}]^{x-}$ , where M<sup>II</sup> is the divalent cation, M<sup>III</sup> is the trivalent cation, A<sup>n-</sup> is an n-valent interlayered anion, z is the moles of water, and x is the ratio M<sup>III</sup>/(M<sup>III</sup> + M<sup>II</sup>).<sup>1,2</sup> The versatility, the diversity of lamellar composition, and the interlamellar anions allow a great variety of applications of these materials.<sup>3–12</sup>

Several reviews dedicated to double lamellar hydroxides have been published, highlighting coprecipitation as a more conventional synthesis method. Most of these works highlight the different synthesis methods, the influence of methods, and synthesis parameters in the formation and structure of LDH. The synthesis parameters evaluated in these studies for the coprecipitation method are pH of synthesis, the base solution's concentration, the nature of the base solution, the aging time and temperature, and the M<sup>2+</sup>/M<sup>3+</sup> molar ratios.<sup>13–15</sup> Almost among all reported applications, LDHs and their derivatives are used as a powder. However, the drying parameter has been neglected. At the end of the synthesis by coprecipitation, the colloidal solution is centrifuged and washed to eliminate any

impurities or pH correction. This step can cause severe agglomerations due to the high humidity before the drying at the end of the process.

From Feitknecht's synthesis in 1933,<sup>16</sup> many other combinations of LDHs started to be synthetically prepared on laboratory, pilot, and industrial scales. However, studies on the drying of the material have not been carried out, and there is no standard for this stage of the synthesis. There are works in the literature with mild drying temperatures such as 40 °C<sup>17,18</sup> and 60 °C<sup>19–21</sup> and intermediate temperatures such as 80 °C<sup>22–25</sup> and above 105 °C.<sup>26,27</sup> Drying times show variations between 12<sup>22</sup> and 24 h<sup>20,26,28</sup> of drying or just information such as "overnight"<sup>24,27,29</sup> or no information.<sup>21,23,30,31</sup>

Different drying parameters and methods can be used to produce different nanoparticles or nanomaterials. To control the nanometric morphology, theoretical research on the drying of nanomaterials is the main focus for the comprehension of the mechanism of degradation of porous structures, colloidal dispersions, nanoparticle agglomeration, and the removal of

Received: July 7, 2021

Accepted: July 29, 2021

Published: August 10, 2021



the solvents during drying.<sup>32,33</sup> Since the performance of solid catalysts is highly dependent on their morphology, surface area, and structure, the preparation of uniform and well-dispersed particles with an optimal composition is of great importance for catalyst development.<sup>34–36</sup> According to Mebrahtu et al.,<sup>35</sup> three main influences govern the performance of bimetallic catalysts derived from hydrotalcite for CO<sub>2</sub> methanation, and one of them is the size of the nanoparticles. The size of the metal nanoparticles affects the preferred reaction mechanism, therefore, in different product selectivities. Anchieta et al.<sup>37</sup> studied the net ionic effect on Ni/ZrO<sub>2</sub> catalysts produced for smelting gas production by methane trireforming and observed that the catalysts used multiple NiO reduction with interactions with the support of different ZrO<sub>2</sub> due to different particle sizes. The most common LDH drying method is freeze-drying. The freeze-dried LDHs exhibiting small (nanosized) crystallites had low crystallinity degrees and retained more anions and molecular water.<sup>38</sup> Solid LDH microspheres were fabricated using a spray drying process, and the effects of process conditions were investigated on agglomerate size distribution, morphology, and specific surface area. As a result, the spherical-shaped agglomerates with smooth surfaces without cracks and holes were formed at all drying conditions.<sup>34,39</sup> Efforts are dedicated to the study and to control the drying of layered double hydroxides. However, most authors are only evaluating the dryer type and not the drying process itself.

Therefore, this study aimed to map the influence of temperature and the drying process time on the synthesis of MgAl/LDH. The drying was assessed using an experimental design as statistical methodology, evaluating the influence of drying time and temperature on the crystallite size and the basal spacing (obtained by XRD analysis). The synthesized material was also characterized by N<sub>2</sub> adsorption/desorption, Fourier transform infrared spectroscopy (FTIR), thermogravimetric analysis (TGA/DTG), and scanning electron microscopy (SEM).

## 2. MATERIALS AND METHODS

**2.1. Materials.** The chemicals magnesium chloride hexahydrate (MgCl<sub>2</sub>·6H<sub>2</sub>O, >99%), aluminum chloride hexahydrate (AlCl<sub>3</sub>·6H<sub>2</sub>O, >99%), and sodium carbonate (NaCO<sub>3</sub>, >99.5%) were purchased from Dinâmica and used as received. Sodium hydroxide (NaOH, >97%) was purchased from Synth. All experimental solutions were prepared using deionized water, which was also used to rinse and clean the samples.

**2.2 LDH Synthesis.** The synthesis was performed according to the coprecipitation method described by Reichle,<sup>16</sup> the most commonly used method.<sup>40</sup> A solution of 203.3 g of MgCl<sub>2</sub>·6H<sub>2</sub>O (1 mol) and 120.7 g of AlCl<sub>3</sub>·6H<sub>2</sub>O (0.5 mol) was diluted in 700 mL of deionized water, maintaining a proportion of 2:1 Mg/Al. To this solution, 280 g of NaOH 50% (3.5 mol) and 100 g of Na<sub>2</sub>CO<sub>3</sub> anhydrous (0.943 mol) were added, diluted in 1000 mL of deionized water. The reaction was performed using a mechanical stirrer (140 rpm) at room temperature. The resulting suspension was maintained under stirring and temperature conditions for 18 h. Then, the suspension was centrifuged, and the materials were washed with deionized water at room temperature until pH reached 10.00. The centrifugation was performed in five steps of 5 min at 5000 rpm, interspersed by washing. The formed colloidal dispersion

was dried in an oven (Tecnal, TE-394/1), as described in the next section.

**2.3 Drying Process: The Experimental Design and Model.** A 2<sup>2</sup> experimental design with four axial points and three repetitions at the central point was used to evaluate the drying parameters' effects, drying time and temperature, on the crystallite size and basal spacing (response parameters). This design is initially organized from a 2<sup>2</sup> factorial design, assays 1–4. Assays 5–7 show three repetitions at the center point, and assays 8–11 represent the axial or star points (Table S1). With the experiments described, it is possible to calculate an empirical model and generate a response surface for the proposed model. Table 1 presents the parameters and coded levels for the drying process, which were defined according to the literature.<sup>19,27,41,42</sup> The experimental design matrix is presented in Table S1.

**Table 1. Parameters and Coded Levels**

drying parameters	coded levels				
	−1.414	−1	0	+1	+1.414
temperature (°C)	68.8	75	90	105	111.2
time (h)	15.2	16	18	20	20.8

The experimental data obtained were evaluated by the response surface regression methodology (RSM), using the second-order polynomial equation (eq 1).

$$y = \beta_0 + \sum_j \beta_j x_j + \sum_{i < j} \beta_{ij} x_i x_j + \sum_j \beta_{jj} x_j^2 + e \quad (1)$$

where  $y$  is the answer (crystallite size and basal spacing),  $x_i$  and  $x_j$  are the independent variables (drying time and temperature) not coded, and  $\beta_0$ ,  $\beta_j$ ,  $\beta_{ij}$ , and  $\beta_{jj}$  are the constant coefficients of interception, linear, quadratic, and interaction, respectively.

**2.4. Characterization.** **2.4.1. N<sub>2</sub> Adsorption/desorption Analysis.** The N<sub>2</sub> adsorption/desorption analysis was conducted for LDHs obtained at 75 °C, 16 h; 105 °C, 16 h; 90 °C, 18 h; 68.8 °C, 18 h; and 112.2 °C, 18 h. The Brunauer–Emmett–Teller (BET) method was used to determine the specific surface area and the Barrett–Joyner–Halenda (BJH) method was used to obtain the pore size and volume. The analysis was performed on a Quantachrome (NOVA 1200) equipment using a sample of 200 mg, submitted to pretreatment in an atmosphere of N<sub>2</sub> at 200 °C for 2 h.

**2.4.2. Fourier Transform Infrared Spectroscopy (FTIR).** FTIR analysis was performed for the materials produced at 75 °C/16 h, 75 °C/20 h, 105 °C/16 h, 105 °C/20 h, and 90 °C/18 h, using a Shimadzu (IRPrestige-21) spectrophotometer. The analysis was conducted in the infrared region's medium ranging from 4000 to 400 cm<sup>−1</sup>, using KBr inserts.

**2.4.3. Thermogravimetric Degradation.** Thermogravimetric analysis for all materials was performed in a simultaneous TGA–DTG apparatus (Shimadzu, ATG-DTG). Approximately, 15 mg of LDH was subjected to a flow of 50 mL/min of synthetic air and a heating ramp of 10 °C/min to 1000 °C.

**2.4.4. X-ray Diffraction.** X-ray diffraction of all materials was performed on a diffractometer Rigaku Multiflex by a powder method, with an incidence of radiation Cu K $\alpha$  ( $\lambda = 1.5406 \text{ \AA}$ ; 40 kV–15 mA), a scan of 2 $\theta$ ° (2–90°), a scanning speed of 2 $\theta$ °/min, and a step of 0.02  $\theta$ °. The results were compared with JCPDS (Joint Committee on Powder Diffraction

Standards) database standards and the literature. The basal spacing can be determined from the Bragg equation (eq 2).

$$n_r \lambda = 2d_{hkl} \sin \theta \quad (2)$$

where  $n_r$  is the order of peak reflection,  $\lambda$  is the X-ray wavelength used,  $d$  is the basal spacing corresponding to the Miller indexes' crystallographic positions ( $hkl$ ), and  $\theta$  is the Bragg angle determined through the peak of the sample.

The LDH typical diffractogram presents basal peaks with Miller indexes  $d_{(001)}$  characteristic for the lamellar material structure and nonbasal peaks with Miller indexes  $d_{(011)}$ ,  $d_{(101)}$ , and  $d_{(111)}$ , related to the layer structure and the stacking sequence. The basal spacing represents the formation of the lamellar layer constituted by the divalent/trivalent cations, provided by an interlamellar layer containing the hydrated anion, neutralizing the charges, and promoting the stacking of the hydroxide layers. The LDHs show characteristic peaks of hydroxide materials with symmetrical reflections for the planes  $d_{(003)}$ ,  $d_{(006)}$ ,  $d_{(009)}$ ,  $d_{(110)}$ , and  $d_{(113)}$ , and asymmetric reflections for nonbasal planes  $d_{(012)}$ ,  $d_{(015)}$ , and  $d_{(018)}$ . The basal planes (001) indicate the degree of crystal growth, while the nonbasal (0kl) suggests failures in the structure stacking.<sup>31,43</sup>

The particle size of the produced LDHs was estimated by Scherrer, Williamson–Hall, and Halder–Wagner. The Scherrer equation is represented by eq 3<sup>44,45</sup>

$$D_s = \frac{K\lambda}{\beta_L \cos \theta} \quad (3)$$

where  $D_s$  is the size of the Scherrer particle (nm),  $K$  is the form factor (approximated to a sphere,  $K = 0.91$ ),  $\lambda$  is the X-ray wavelength used,  $\beta_L$  is the width at the peak half-height, and  $\theta$  is the Bragg angle.

The Williamson–Hall model (eq 7) was proposed to address the limitations of the Scherrer equation, based on approximate formulas for the width at the peak half-height,  $\beta_L$  (eq 4), and the widening of deformation,  $\beta_e$  (eq 5). The Halder–Wagner method (eq 8) determines the crystallite size when the deformation anisotropy is low.

$$\beta_L = \frac{K\lambda}{D_s \cos \theta} \quad (4)$$

$$\beta_e = C_p \varepsilon \tan \theta \quad (5)$$

$$\beta_{\text{tot}} = \beta_L + \beta_e \quad (6)$$

$$\beta_{\text{tot}} \cos \theta = \varepsilon_{\text{WH}} \sin \theta + \frac{K\lambda}{D_{\text{WH}}} \quad (7)$$

$$\left( \frac{\beta_{\text{tot}} \cos \theta}{\sin \theta} \right)^2 = \frac{K\lambda}{D_{\text{HW}}} \cdot \frac{\beta_{\text{tot}} \cos \theta}{\sin^2 \theta} + 16\varepsilon_{\text{HW}}^2 \quad (8)$$

where  $C_p$  is the proportionality constant to convert the integral amplitude of the deformation distribution into microdeformation.  $\varepsilon_{\text{WH}}$  and  $D_{\text{WH}}$  are the microdeformation and particle size determined by the Williamson–Hall model, respectively.  $\varepsilon_{\text{HW}}$  and  $D_{\text{HW}}$  are the microdeformation and particle size determined by the Halder–Wagner method.

Network parameters “ $a$ ” and “ $c$ ” were calculated according to Pérez-Ramírez et al. The layered parameter “ $a$ ” provides the average distance between the cations in the lamella and can be calculated by eq 9. The parameter “ $c$ ” is related to the brucite

lamella thickness and the interlamellar distance, calculated by eq 10. This calculation is appropriate if the  $d_{(001)}$  reflections are clear. However, if the peaks are wide, parameter “ $c$ ” can be obtained by the average position of the diffraction peaks corresponding to  $d_{(003)}$ ,  $d_{(006)}$ , and  $d_{(009)}$  planes, according to eqs 11 and 12.

$$a = 2d_{(110)} \quad (9)$$

$$c = 3d_{(003)} \quad (10)$$

$$c = \frac{3}{2}(d_{(003)} + 2d_{(006)}) \quad (11)$$

$$c = \frac{3}{2}(d_{(003)} + 2d_{(006)} + 3d_{(009)}) \quad (12)$$

**2.4.5. Scanning Electron Microscopy (SEM).** SEM analyses were conducted for the materials produced at 75 °C, 16 h; 105 °C, 16 h; 90 °C, 18 h; 68.8 °C, 18 h; and 112.2 °C, 18 h. The samples were previously covered with gold using a metallizer (Sanyu Electron, Quick Coater SC-701), metallization for 6 min with a gold target at 10 mA. SEM analyses were performed using an electronic scanning microscope (Shimadzu, SSX-550 Superscan), with an acceleration voltage of 20kV.

### 3. RESULTS AND DISCUSSIONS

**3.1. Characterization.** **3.1.1.  $N_2$  Adsorption/desorption Analysis.** Figure 1 shows the  $N_2$  adsorption/desorption

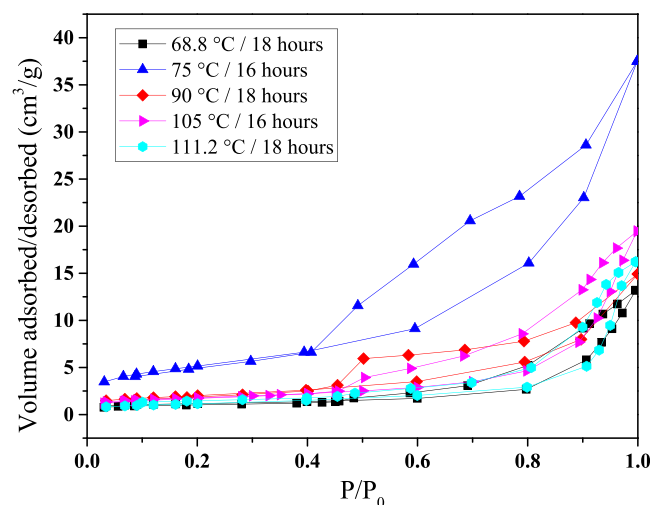


Figure 1.  $N_2$  adsorption/desorption isotherms.

isotherms for LDHs obtained at 75 °C, 16 h; 105 °C, 16 h; 90 °C, 18 h; 68.8 °C, 18 h; and 112.2 °C, 18 h. These isotherms are directly associated with LDHs' porosity. All isotherms obtained showed similarities with type IV, according to the IUPAC classification.<sup>46</sup> The smooth increase at low pressure represents the formation of a monolayer or mesoporosity. A sharp improvement at relatively high pressure evinces that condensation occurs, betoken mesoporosity.<sup>1,47</sup>

Type IV isotherm denotes that capillary condensation occurs and causes hysteresis, becoming more pronounced when the pores' dispersion is extensive.<sup>46</sup> The loops of hysteresis are H3 type (according to IUPAC), present in nonrigid aggregates of particles similar to parallel plates. This loop structure can convey information related to pores' geometry and distribution. The materials obtained presented the average pore

diameter characteristic of the mesoporous structure. The textural properties, surface areas, pore volume, and average pore diameter are shown in Table 2.

**Table 2. Textural Properties**

temperature (°C)	surface area (m <sup>2</sup> /g)	pore volume (cm <sup>3</sup> /g)	average pore diameter (nm)
68.8	4.09	0.02	20.0
75	18.6	0.06	12.5
90	7.16	0.02	12.9
105	6.31	0.03	19.1
111.2	4.10	0.02	24.5

Xue et al.<sup>48</sup> obtained a specific surface area of 3.9 m<sup>2</sup>/g for a sample of biochar/MgFe-LDH, a value within the range of Table 2. According to the authors, this surface area value is in the typical LDH range for a component, like MgAl-LDH.

Due to the sintering process, phenomena that occur during heating that lead to the powder's densification; a decrease in the surface area of LDHs is observed for temperatures above 75 °C. It can be observed that the average pore diameter presents an opposite tendency, decreasing with the elevation of the temperature. The macroscopic driving force that operates during the sintering process reduces excess energy associated with the material surface, as in other irreversible processes. This energy reduction occurred through the atomic process of sintering governed by the coarsening process, with an increase in the pore diameter. Santos et al.<sup>49</sup> reported that the pore distribution is related to the formation method and the ions in the layer, while the pore size is related to the synthesis and connection between the LDH lamellae. Changes in particles' shape can also occur over time, usually increasing the average grain size.<sup>1,2</sup>

The surface area for a temperature of 68.8 °C may have been caused by residual sodium chloride in the synthesis of lamellar double hydroxides. The residual presence can hold the diffusive advance of the atoms in increasing the surface area, in addition to the presence of possible micropores in the material. The micropore volume was calculated using the Dubinin-Radushkevich method, and it was not possible to observe the presence of micropores. Nitrogen adsorption is generally accepted as the standard method for micropore and mesopores size analysis. The quadrupolar nature of the nitrogen molecule is responsible for the interaction of functional groups on the surface of exposed materials and ions. In this way, N<sub>2</sub> molecules can block micropore entrances, causing pore filling pressure not to be correlated with pore size/structure.<sup>46,50</sup>

**3.1.2. Fourier Transform Infrared Spectroscopy (FTIR).** All of the obtained FTIR spectra presented the set of hydrotalcite characteristic bands, and the spectra for MgAl/LDH are shown in Figure 2. The results allowed a better understanding of vibrational modes as a function of the drying methodology used. The vibration bands around 3440 and 3000 cm<sup>-1</sup> can be attributed to the O-H stretch of hydroxyl groups, interlamellar water molecules, and physically adsorbed water. The band of 3000 cm<sup>-1</sup> is related to the hydrogen bond of H<sub>2</sub>O to CO<sub>3</sub><sup>2-</sup> ions at the interlamellar space. In addition to the influence of water molecules, there is an enlargement of the band at 3440 cm<sup>-1</sup>, indicating hydrogen-bound hydroxyl radicals. The band at 1640 cm<sup>-1</sup> is mainly due to the HOH stretch physically adsorbed.<sup>51</sup> The band around 2350 cm<sup>-1</sup> is due to the

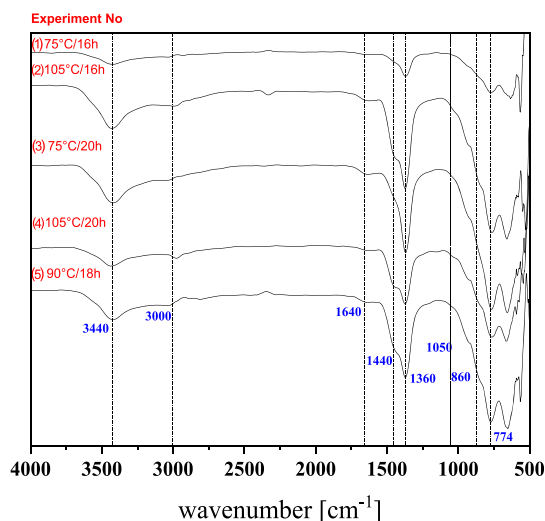


**Figure 2.** FTIR spectra.

atmospheric background noise used in the measurement system.<sup>19,52</sup> The various assignments for each band are summarized in Table S2.

The carbonate ion (CO<sub>3</sub><sup>2-</sup>) can be found in more than one atomic species in the LDH interlamellar layer. The bands corresponding to the presence of CO<sub>3</sub><sup>2-</sup>, characterized by a D<sub>3h</sub> trigonal planar symmetry, present the vibrations ν<sub>2</sub>, ν<sub>3</sub>, and ν<sub>4</sub> that appear at 860, 1360, and 774 cm<sup>-1</sup>, respectively.<sup>51,53</sup> These vibrational bands are related to the different forms of CO<sub>3</sub><sup>2-</sup> anion interaction. It is possible to observe three bands' overlapping (Supporting Information, Figure S1) in the carbonate region, 1200–1800 cm<sup>-1</sup>, which features different basicities on the LDH surface. The small band at 1050 cm<sup>-1</sup> confirms the bands' superposition regarding three species of carbonates.<sup>54,55</sup>

The formed carbonate species refer to bicarbonate, monodentate, and bidentate carbonates. Three hypotheses could be made considering the CO<sub>3</sub><sup>2-</sup> anion interactions: the first is the formation of free anions or adsorbed anions on the LDH outer layers' surface, the second is the interaction between the anion and the hydrogen of the interlamellar water, and the third one is the interaction between the anion with the hydroxyl.<sup>56,57</sup>

Bicarbonates are formed on the surface from the interaction between the anion and hydroxyl radicals (considered weak Bronsted basic sites). Rege and Yang<sup>58</sup> observed for γ-alumina the bands of bicarbonate at 3605, 1640, 1480, and 1235 cm<sup>-1</sup>. According to the coordination of oxygen atoms and interaction with the metallic sites, they form monodentate (considered strong Lewis basic sites) and or bidentate (intermediate characteristics of Lewis acid–base) carbonates. The spectra indicate that there is the formation of bridge bidentate carbonates at 1360 cm<sup>-1</sup>.

Bands around 1440 cm<sup>-1</sup> are also attributed to the vibrations of ν<sub>3</sub> (CO<sub>3</sub><sup>2-</sup>) groups, suggesting a lower symmetry of carbonate groups than D<sub>3h</sub>, characteristic of (CO<sub>3</sub><sup>2-</sup>) free ions, relatively undistorted and possibly in the surface.<sup>52,59–61</sup> The high intensity of the vibrational band at 1360 cm<sup>-1</sup> suggests a high amount of low symmetry carbonate in the interlamellar space.<sup>51</sup> The carbonate is no longer determined by the hydrotalcite structure but by the interactions with metal ions in the mixed oxide phase.

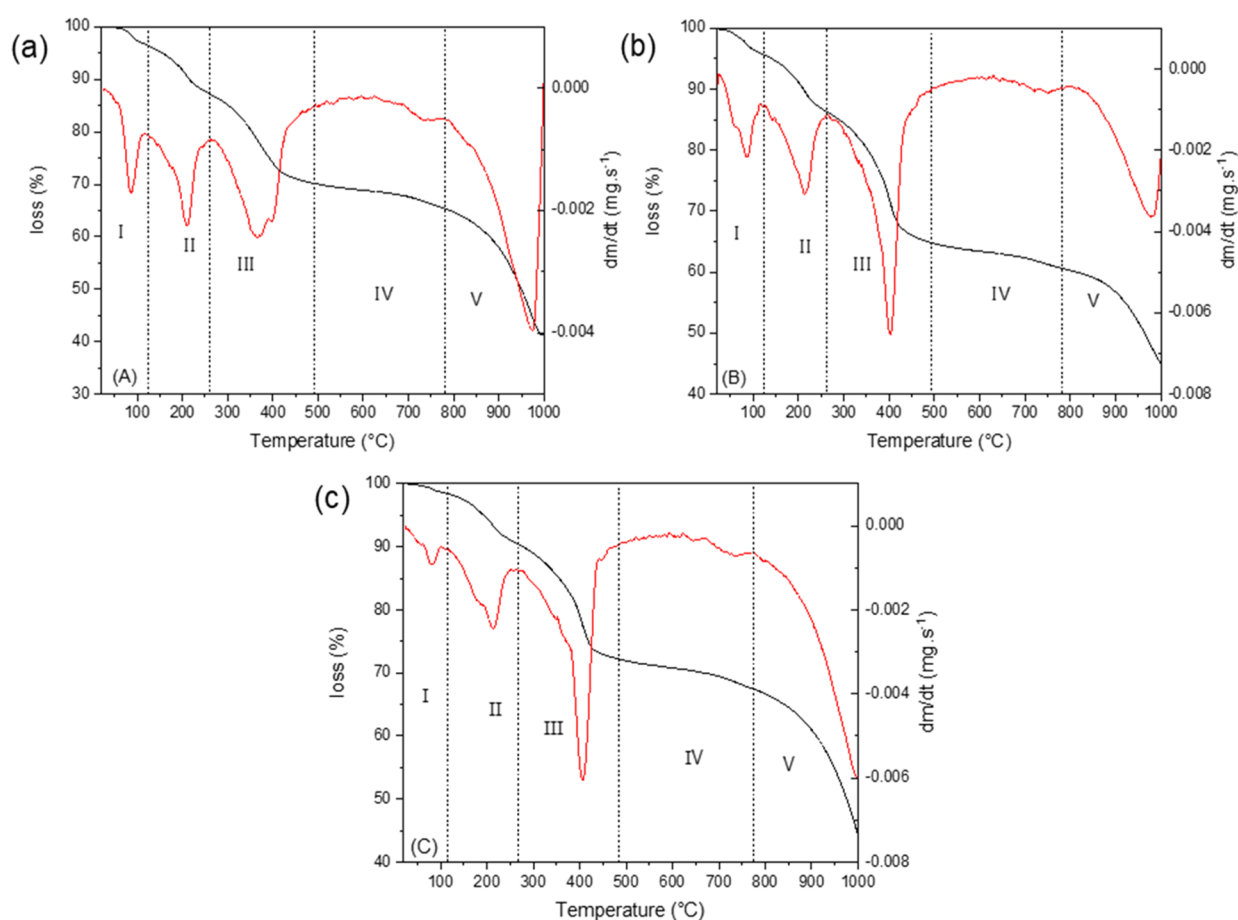


**Figure 3.** TGA/DTG analysis: (a) 75 °C, 20 h; (b) 90 °C, 18 h; and (c) 105 °C, 20 h.

The bands between 400 and 800  $\text{cm}^{-1}$  may be due to the superposition of magnesium and aluminum oxides' vibrational absorptions. In this way, peaks around 660 can be attributed to the Mg–O or Al–O band.<sup>61,62</sup> Thus, several active sites with different basic properties can be formed on the LDH surface according to the drying temperature employed, contributing to this study's relevance.

**3.1.3. Thermogravimetric Degradation.** Thermogravimetric (TGA) and differential thermal analysis (DTG) curves are presented in Figure 3. Complete data about the 11 experiments are shown in Table S3. The decomposition zones may vary according to the cations' nature and proportion, the interlamellar anion, and the material crystallinity. In general, LDHs containing carbonate as interlamellar anion presents three stages of thermal transition, whose properties (temperature and intensity) vary according to the lamellar layer's aluminum content. The thermal decomposition of hydroxalcite is a complex sequence of dehydration, dehydroxylation, and decarbonization of the initial material, being attributed to the loss of water between the lamellae, structural hydroxyl groups (such as  $\text{H}_2\text{O}$ ), and interlamellar carbonates, respectively.<sup>63–66</sup> This mass loss and disruption processes are essential in producing oxide and catalysts supported by oxide.<sup>67</sup>

The MgAl/LDH thermal decomposition process can be divided into five zones:<sup>68</sup> zone I—initial mass loss, below 100 °C; zone II—in the range of 100–265 °C, corresponding to dehydration, removal of water from the LDH structure; zone III—with two components, at approximately 340 and 410 °C, dehydroxylation and decarbonization, respectively; zones IV

and V—associated with the formation of  $\text{MgAl}_2\text{O}_4$  spinel and solid solutions composed of Mg–Al. The results obtained for the 11 experiments corroborate those reported in the literature.<sup>6,64,69,70</sup>

In zone I, this process occurs between room temperature and temperature of 100 °C and usually presents a mass loss between 1 and 2%. Nevertheless, although drying at 105 °C is sufficient to remove this water, exposure to environmental conditions (even during sample handling) is enough for partial external rehydration of the sample, giving rise to water resorption. It is verified in Table S3 that the amount of reabsorbed water varies according to temperature and drying time and is related to the surface area and porosity of the materials. Larger surface areas promote a higher amount of adsorbed water.<sup>63</sup> In zone II, the water between layers is responsible for the weight loss of around 220 °C, with two consecutive stages. The first, up to 140–180 °C, the intermediate layer is dehydrated. The second stage, up to 240–260 °C, is regarding the dehydrated phase's total formation.<sup>64,71,72</sup>

Mahjoubi et al.<sup>20</sup> performed thermogravimetric characterization (TGA–DTA) for ZnAl–LDH interspersed with  $\text{CO}_3^{2-}$ ,  $\text{NO}_3^-$ ,  $\text{Cl}^-$ , or  $\text{SO}_4^{2-}$  and found values similar to those observed in Table S3. All LDH standards showed a loss between 10 and 14% due to water loss from the interlayer layer in the temperature range between 50 and 250 °C (zone I and zone II). ZnAl– $\text{CO}_3$  presented dehydration in two stages, at 150 and 250 °C. The total loss of mass was 20.86%.

These two processes are responsible for the observed mass loss up to 450–500 °C, varying according to the sample's chemical nature. The dehydroxylation of OH linked to the aluminum cation present inside the lamella is attributed to the peak around 305–320 °C, while the peak at 375–400 °C is attributed to the dehydroxylation of OH bounded with a magnesium cation and the main decarbonation by CO<sub>2</sub>.<sup>63,64</sup> The different obtained profiles related to the drying temperature suggest the rearrangement of the CO<sub>3</sub> groups in the region of 400–580 °C.<sup>73</sup> This stage is related to decarbonation and the different basic sites present in the materials. For this reason, there are changes in the DTG profiles.<sup>6,63</sup>

**3.1.4. X-ray Diffraction.** The XRD analysis was performed for all materials. The samples' patterns exhibit the characteristic reflections of layered double hydroxides, as shown in Figure 4. The diffraction peaks were indexed to a hexagonal

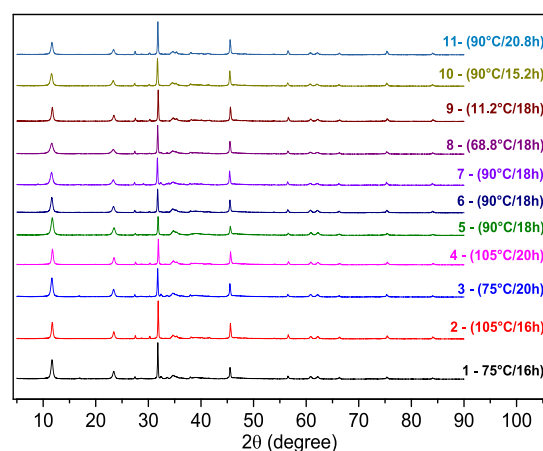


**Figure 4.** X-ray diffractogram for all materials.

lattice with a rhombohedral 3R symmetry.<sup>20</sup> The peaks' intensity and width made it possible to determine some characteristics, such as the basal spacing, degree of crystallinity, network parameters, an organization regarding the lamellar stacking, and the average size LDH crystallites.

The basal spacings  $d_{(003)}$  and  $d_{(006)}$ , parameter "c" related to the lamellar stacking and basal spacing, and the parameter "a" referring to the distance between metal ions in the lamellar layer are arranged in Table 3. The results show that the change in the drying step produced LDHs with variations in the basal spacing and the network parameter "c".

The network parameter "a" calculated according to eq 9 does not change significantly as expected. All LDHs produced are of the hydrotalcite type and contain Mg/Al in their lamella layer, which does not change the ionic distance.

According to some authors, LDHs undergo variation in their basal spacing at temperatures above 210 °C. Mahjoubi et al.<sup>20</sup> synthesized zinc aluminum layered double hydroxides intercalated with carbonate, nitrate, chloride, or sulfate via a coprecipitation method. The LDH samples were dried at 60 °C for 24 h, and the interlamellar distance  $d_{(003)}$  of the ZnAl-CO<sub>3</sub> was found to be 7.57 Å. Moriyama et al.<sup>38</sup> obtained different values for the basal spacing  $d_{(003)}$  between 7.56 and 7.76 Å, using two drying methods at temperatures below 150 °C. In addition, according to Han et al.,<sup>74</sup> parameter "c" also relates the ionic radius of the interlamellar anions to the electrostatic force between these anions and the hydroxyls of the lamellar layer.

**Table 3.** Basal Spacing Values and Network Parameters According to the Experimental Design

assay	basal spacing (Å)		network parameters (Å)	
	$d_{003}$	$d_{006}$	a	c
1 (75 °C/16 h)	7.58	3.80	3.04	22.76
2 (105 °C/16 h)	7.55	3.80	3.04	22.71
3 (75 °C/20 h)	7.59	3.80	3.05	22.80
4 (105 °C/20 h)	7.52	3.79	3.04	22.65
5 (90 °C/18 h)	7.55	3.79	3.04	22.70
6 (90 °C/18 h)	7.60	3.81	3.05	22.83
7 (90 °C/18 h)	7.64	3.82	3.05	22.91
8 (68.8 °C/18 h)	7.62	3.82	3.05	22.88
9 (111.2 °C/18 h)	7.54	3.80	3.04	22.70
10 (90 °C/15.2 h)	7.64	3.89	3.05	22.91
11 (90 °C/20.8 h)	7.59	3.81	3.05	22.80

An experimental design was used to analyze parameter "c" values and the basal spacings  $d_{(003)}$  and  $d_{(006)}$  as a function of drying time and temperature. A response surface presenting this behavior is shown in Figure 5. It is observed that the spacings  $d_{(003)}$  and  $d_{(006)}$  showed a decrease in size with increasing temperature and drying time. A reduction of parameter "c" was observed due to the increase in drying time and temperature, directly influenced by the nature of the intercalated anion, moisture, and the cation load in the lamella.<sup>75</sup> Depending on the degree of LDH hydration, the basal spacing may vary, directly influencing the parameter "c" value. This parameter is related to the lamellar layer thickness and the distance between these lamellae. Therefore, the same behavior is expected for the basal spacing. One factor that can affect the decrease in the basal spacing and the network parameter "c" and the degree of hydration is the electrostatic interactions between the cations.

Through the intensity and width of the peaks, it was possible to determine the average crystallite sizes of the LDHs. The values resulted from peaks  $d_{(003)}$ ,  $d_{(006)}$ ,  $d_{(012)}$ ,  $d_{(015)}$ , and  $d_{(018)}$ , from the LDH lamellar structure, and from the peaks  $2\theta = 31,79^\circ$  and  $2\theta = 45,60^\circ$ , resulting from the impurity related to the sodium chloride. Due to its ionic characteristic, chloride often presents residues in the final material structure.<sup>19,30,31</sup> The results were calculated using eqs 3, 7, and 8 from the Scherrer, Williamson–Hall, and Halder–Wagner methods, respectively, presented in Table 4.

Figure 6 shows the response surfaces obtained from the experimental design. Due to the sintering process, crystals' growth with increased temperature was already expected.<sup>50,76</sup> LDH crystallite average sizes were observed between 12.19 nm (assay 8) and 60.95 nm (assay 2), varying with drying time and temperature, as well as the method used for the calculation. Moriyama et al.<sup>38</sup> obtained crystallite sizes of NO<sub>3</sub>-LDH, and Cl-LDH ranging from 93.0 to 97.1 nm for the materials dried at 100 °C and from 61.1 to 64.9 nm for the freeze-dried.

Thus, the grains becoming higher as a function of the increase in temperature due to the atomic densification process favored in LDH sintering. Low temperatures and longer drying times favor the densification mechanism, causing a reduction in the material porosity (Figure 1).

With the results, it was possible to perform the analysis of variance (ANOVA), Table S4. The experimental design evaluated both the linear, quadratic, and interaction terms regarding drying time and temperature for LDH synthesis.

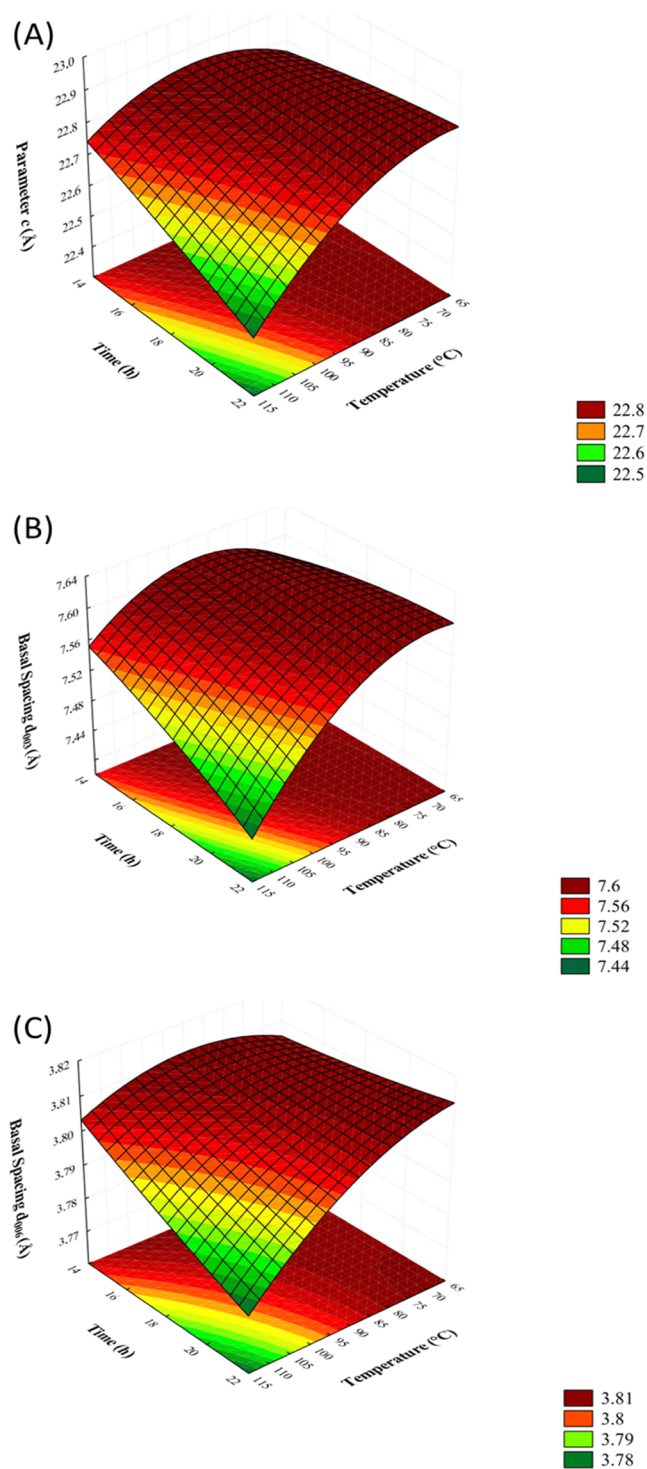


**Figure 5.** Response surface for parameter “c” (A) and basal spacings  $d_{003}$  (B), and  $d_{006}$  (C).

The adjusted empirical models, also known as a complete fitted model, are characterized by eq 13 (Scherrer model), eq 14 (Williamson–Hall model), and eq 15 (Halder–Wagner model), where  $y$  is the LDH crystallite size. Due to the significant variability inherent to the structural degradation of nanomaterials regarding the capillary pressure, a significance level of  $\alpha = 0.10$  was used.

**Table 4.** Size of LDH Crystallites in Nanometers According to the Model Used

assay	Scherrer	Williamson–Hall		Halder–Wagner	
	size (nm)	size (nm)	deformation	size (nm)	deformation
1	26.75	22.98	0.00	19.74	0.01
2	33.21	60.95	0.01	16.89	0.01
3	26.28	31.86	0.01	16.30	0.01
4	29.42	30.48	0.00	21.24	0.01
5	23.21	18.21	0.00	16.69	0.01
6	27.80	26.45	0.00	16.49	0.01
7	24.05	14.60	0.00	15.93	0.01
8	23.18	12.19	0.00	13.10	0.01
9	29.34	38.94	0.01	19.47	0.01
10	25.45	21.57	0.00	17.31	0.01
11	37.47	35.05	0.00	16.11	0.01

$$y = 25.020 + 2.2896 \cdot T + 0.6344 \cdot T^2 + 1.5911 \cdot t + 3.2336 \cdot t^2 - 0.8308 \cdot T \cdot t \quad (13)$$

$$y = 19.754 + 9.3021 \cdot T + 5.3142 \cdot T^2 - 0.3167 \cdot t + 6.6849 \cdot t^2 - 9.8393 \cdot T \cdot t \quad (14)$$

$$y = 16.371 + 1.3865 \cdot T + 0.4691 \cdot T^2 - 0.0977 \cdot t + 0.68137 \cdot t^2 + 1.9488 \cdot T \cdot t \quad (15)$$

The models did not present a good fit with the experimental data. The coefficients of determination values were lower than 0.8, with Williamson–Hall presenting the highest value, with 0.7484. This can be attributed to the fact that other parameters may directly influence the sintering process and pore formation in addition to temperature and time. The F test results (Table S4) demonstrate that the models are unsuitable for making statistical predictions. Scherrer and Williamson–Hall models did not present a lack of adjustment; the models’ inability to adjust to the values is confused with the error in the central point’s authentic replicas. Since the Scherrer, Williamson–Hall, and Halder–Wagner models present their limitations to calculate the nanostructured materials’ size, the models lack adjustment and no significance was expected. Although these are the models used to determine particle size, they underestimate the size in calculation. Development of methods that determine particle sizes in nanocrystalline powders is still in progress.<sup>45,77</sup>

With the results obtained for parameter “c” and basal spacing  $d_{(003)}$ , variance analysis was also performed, constructing an ANOVA table (Table S5). The empirical models for parameter “c” and basal spacing are represented by eqs 16 and 17, respectively.

$$c = 22.813 - 0.0568 \cdot T - 0.0348 \cdot T^2 - 0.0220 \cdot t - 0.0022 \cdot t^2 - 0.025 \cdot T \cdot t \quad (16)$$

$$d_{(003)} = 7.599 - 0.0228 \cdot T - 0.0182 \cdot T^2 - 0.0107 \cdot t - 0.0020 \cdot t^2 - 0.0108 \cdot T \cdot t \quad (17)$$

The models presented low values of coefficients of determination, with no good agreement with the experimental data. The F test results (Table S5) demonstrate that the models are unsuitable for making statistical predictions. However, F’ results for the quadratic means of the lack of adjustment and pure error showing that these quadratic means

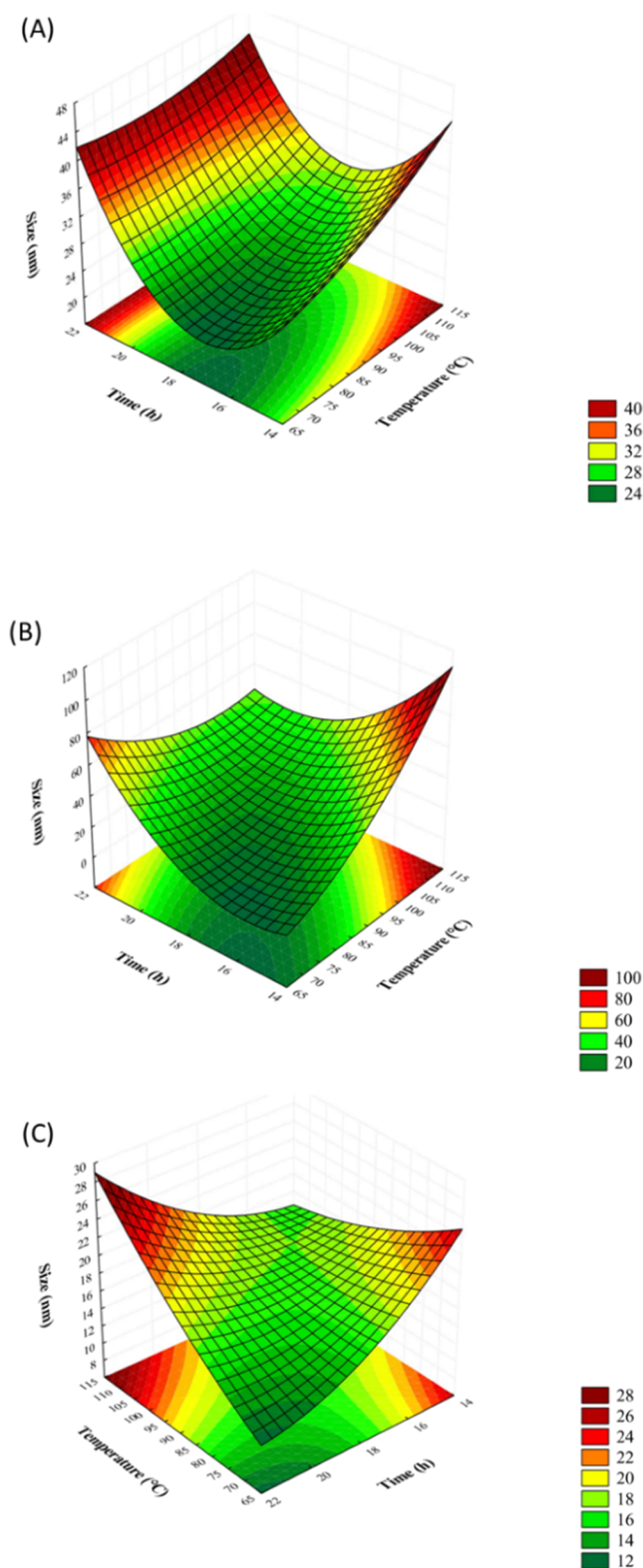


**Figure 6.** Response surface for the crystallite size. (A) Scherrer, (B) Williamson–Hall, and (C) Halder–Wagner.

are statistically equal and confused, stating that the model does not demonstrate a lack of adjustment. Figure 5 shows a decrease in parameter “ $c$ ” and basal spacing  $d_{(003)}$  according to the increase in temperature, which is physically consistent and is confirmed by the empirical models. In eqs 16 and 17, the coefficients’ values are negative, and the basal spacing and

parameter “ $c$ ” values are inversely proportional to the drying time and temperature.

Yang et al.<sup>68</sup> presented the thermal evolution of the structural MgAl–CO<sub>3</sub>/LDH in the calcination process. There is a decrease in the basal spacing and in the parameter “ $c$ ” when the material leaves the temperature of 70–190 °C, corroborating with the results collected in this work, where there is a decrease in the basal spacing due to the removal of interlayer water by the increase in drying temperature.

**3.1.5. Scanning Electron Microscopy (SEM).** Figure 7 presents the SEM images for the materials produced at 75 °C,

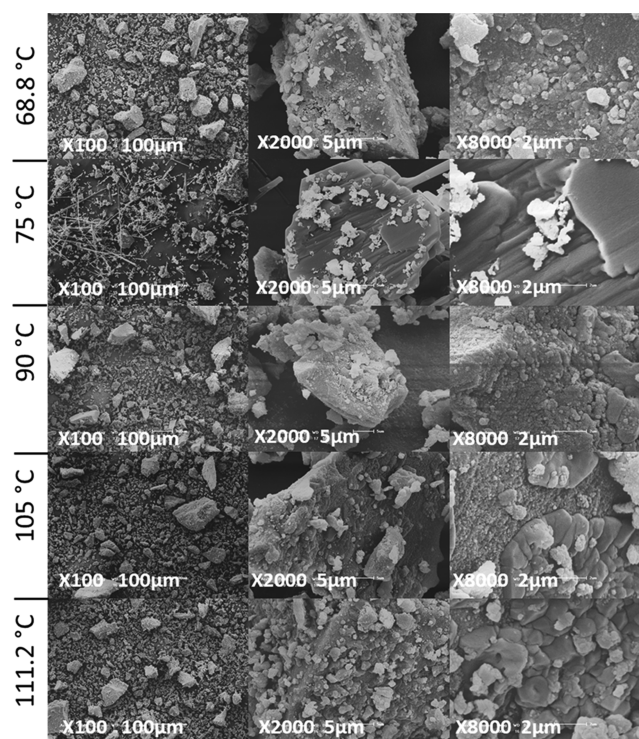


**Figure 7.** LDH SEM images.

16 h; 105 °C, 16 h; 90 °C, 18 h; 68.8 °C, 18 h; and 112.2 °C, 18 h. Hydrotalcites present developed, thin, flat crystals with obvious edges indicating the layered structure.<sup>78</sup> In general, the materials showed particles with irregular grains, the elevation of aggregates with the increase in drying temperature, which can corroborate the significant decrease in the specific surface area, and the increase in the average crystallites sizes.<sup>79</sup>

#### 4. CONCLUSIONS

This work presented that drying time and temperature modifications alter the chemical, physical, structural, and textural properties of MgAl layered double hydroxide. The results showed that changes in the drying stage produced LDHs with variation in the basal spacing and network parameter “ $c$ ”. Although it has been reported in the literature that temperatures below 210 °C do not affect the basal spacing, the decrease in the parameter “ $c$ ” and the basal spacing ( $d_{003}$ ) with increasing temperature is physically consistent, and this is due to the existence of free water molecules between the anion and the coverslip. FTIR and TG analyses evidenced changes in the basic sites of LDH from the drying process. Through the X-ray analysis and the use of the Scherrer, Williamson–Hall, and Halder–Wagner methods, it was possible to observe the

tendency of the crystallite size growth, as well as the structural modification. Finally, this study provides important information regarding the influence of drying parameters on the LDHs' structural characteristics. Therefore, controlling the drying time or temperature can obtain materials with particular and desirable properties for specific applications, as catalysts where the physical–chemical properties of the materials influence the catalytic performance.

## ■ ASSOCIATED CONTENT

### SI Supporting Information

The Supporting Information is available free of charge at <https://pubs.acs.org/doi/10.1021/acsomega.1c03581>.

Deconvolution of overlapping bands in the carbonate region in the sample dried (a), experiment 3 (75 °C), (b) experiment 5 (90 °C), and (c) experiment 4 (105 °C) (Figure S1); matrix of experimental assays (Table S1); frequency ( $\text{cm}^{-1}$ ) of the FTIR spectrum according to the attributions in Figure 2 (Table S2); mass loss determined by thermal analysis (Table S3); ANOVA for models of medium size crystallites (Table S4); and ANOVA for parameter  $c$  and basal spacing (Table S5) (PDF)

## ■ AUTHOR INFORMATION

### Corresponding Author

Lucas Meili – Laboratory of Processes, Center of Technology, Federal University of Alagoas (UFAL), Maceió, Alagoas 57072-900, Brazil; [orcid.org/0000-0002-0307-8204](https://orcid.org/0000-0002-0307-8204); Email: [lucas.meili@ctec.ufal.br](mailto:lucas.meili@ctec.ufal.br)

### Authors

Luiz D. Silva Neto – Drying Center of Pastes, Suspensions, and Seeds, Department of Chemical Engineering, Federal University of São Carlos (UFSCar), São Carlos, São Paulo 13565-905, Brazil; [orcid.org/0000-0002-7945-937X](https://orcid.org/0000-0002-7945-937X)

Chayene G. Anchieta – Advanced Energy Storage Division, Laboratory of Advanced Batteries (LAB), Center for Innovation on New Energies, School of Chemical Engineering, University of Campinas (Unicamp), Campinas, São Paulo 13083-852, Brazil

José L. S. Duarte – Laboratory of Processes, Center of Technology, Federal University of Alagoas (UFAL), Maceió, Alagoas 57072-900, Brazil

José T. Freire – Drying Center of Pastes, Suspensions, and Seeds, Department of Chemical Engineering, Federal University of São Carlos (UFSCar), São Carlos, São Paulo 13565-905, Brazil

Complete contact information is available at: <https://pubs.acs.org/doi/10.1021/acsomega.1c03581>

### Author Contributions

This manuscript was written through the contributions of all authors. All authors have given approval to the final version of the manuscript.

### Funding

This work was supported by the Conselho Nacional de Desenvolvimento Científico e Tecnológico (CNPq/Brazil), Coordenação de Aperfeiçoamento de Pessoal de Nível Superior (CAPES/Brazil), and Fundação de Amparo à Pesquisa do Estado de Alagoas (FAPEAL/Brazil).

## Notes

The authors declare no competing financial interest.

## ■ REFERENCES

- (1) de Souza dos Santos, G. E.; Ide, A. H.; Duarte, J. L. S.; McKay, G.; Silva, A. O. S.; Meili, L. Adsorption of Anti-Inflammatory Drug Diclofenac by MgAl/Layered Double Hydroxide Supported on Syagrus Coronata Biochar. *Powder Technol.* **2020**, *364*, 229–240.
- (2) Zümreoglu-Karan, B.; Ay, A. N. Layered Double Hydroxides - Multifunctional Nanomaterials. *Chem. Pap.* **2012**, *66*, 1–10.
- (3) Kameda, T.; Takeuchi, H.; Yoshioka, T. Hybrid Inorganic/Organic Composites of Mg-Al Layered Double Hydroxides Intercalated with Citrate, Malate, and Tartrate Prepared by Co-Precipitation. *Mater. Res. Bull.* **2009**, *44*, 840–845.
- (4) Kameda, T.; Uchiyama, T.; Yoshioka, T. Equilibrium and Kinetics Studies on the Adsorption of Substituted Phenols by a Cu-Al Layered Double Hydroxide Intercalated with 1-Naphthol-3,8-Disulfonate. *J. Alloys Compd.* **2016**, *670*, 322–328.
- (5) Kooli, F.; Jones, W.; Rives, V.; Ulibarri, M. A. An Alternative Route to Polyoxometalate- Exchanged Layered Double Hydroxides: The Use of Ultrasound. *J. Mater. Sci. Lett.* **1997**, *16*, 27–29.
- (6) Labajos, F. M.; Rives, V.; Ulibarri, M. A. Effect of Hydrothermal and Thermal Treatments on the Physicochemical Properties of Mg-Al Hydrotalcite-like Materials. *J. Mater. Sci.* **1992**, *27*, 1546–1552.
- (7) Leroux, F.; Taviot-Guého, C. Fine Tuning between Organic and Inorganic Host Structure: New Trends in Layered Double Hydroxide Hybrid Assemblies. *J. Mater. Chem.* **2005**, *15*, 3628–3642.
- (8) Roland-Swanson, C.; Besse, J.-P.; Leroux, F. Polymerization of Sulfopropyl Methacrylate, a Surface Active Monomer, within Layered Double Hydroxide. *Chem. Mater.* **2004**, *16*, 5512–5517.
- (9) Vaysse, C.; Guerlou-Demourgues, L.; Duguet, E.; Delmas, C. Acrylate Intercalation and in Situ Polymerization in Iron-, Cobalt-, or Manganese-Substituted Nickel Hydroxides. *Inorg. Chem.* **2003**, *42*, 4559–4567.
- (10) Coronado, E.; Martí-Gastaldo, C.; Navarro-Moratalla, E.; Ribera, A. Confined Growth of Cyanide-Based Magnets in Two Dimensions. *Inorg. Chem.* **2010**, *49*, 1313–1315.
- (11) Khan, A. I.; Lei, L.; Norquist, A. J.; O'Hare, D. Intercalation and Controlled Release of Pharmaceutically Active Compounds from a Layered Double Hydroxide. *Chem. Commun.* **2001**, *21*, 2342–2343.
- (12) Rives, V.; del Arco, M.; Martín, C. Intercalation of Drugs in Layered Double Hydroxides and Their Controlled Release: A Review. *Appl. Clay Sci.* **2014**, *88–89*, 239–269.
- (13) Theiss, F. L.; Ayoko, G. A.; Frost, R. L. Synthesis of Layered Double Hydroxides Containing Mg<sup>2+</sup>, Zn<sup>2+</sup>, Ca<sup>2+</sup> and Al<sup>3+</sup> Layer Cations by Co-Precipitation Methods - A Review. *Appl. Surf. Sci.* **2016**, *383*, 200–213.
- (14) Bukhtiyarova, M. V. A Review on Effect of Synthesis Conditions on the Formation of Layered Double Hydroxides. *J. Solid State Chem.* **2019**, *269*, 494–506.
- (15) Santos, G. E.; de, S.; Lins, P. V.; dos, S.; Oliveira, L. M. T.; de, M.; Silva, E. O.; da Anastopoulos, I.; Erto, A.; Giannakoudakis, D. A.; Almeida, A. R. F.; de Duarte, J. L.; da, S.; Meili, L. Layered Double Hydroxides/Biochar Composites as Adsorbents for Water Remediation Applications: Recent Trends and Perspectives. *J. Clean. Prod.* **2021**, *284*, No. 124755.
- (16) Reichle, W. T. Catalytic Reactions by Thermally Activated, Synthetic, Anionic Clay Minerals. *J. Catal.* **1985**, *94*, 547–557.
- (17) Khodam, F.; Rezvani, Z.; Amani-Ghadim, A. R. Enhanced Adsorption of Acid Red 14 by Co-Assembled LDH/MWCNTs Nanohybrid: Optimization, Kinetic and Isotherm. *J. Ind. Eng. Chem.* **2015**, *21*, 1286–1294.
- (18) Chitrakar, R.; Makita, Y.; Sonoda, A.; Hirotsu, T. Fe-Al Layered Double Hydroxides in Bromate Reduction: Synthesis and Reactivity. *J. Colloid Interface Sci.* **2011**, *354*, 798–803.
- (19) Meili, L.; Lins, P. V.; Zanta, C. L. P. S.; Soletti, J. I.; Ribeiro, L. M. O.; Dornelas, C. B.; Silva, T. L.; Vieira, M. G. A. MgAl-LDH/Biochar Composites for Methylene Blue Removal by Adsorption. *Appl. Clay Sci.* **2019**, *168*, 11–20.

- (20) Mahjoubi, F. Z.; Khalidi, A.; Abdennouri, M.; Barka, N. Zn–Al Layered Double Hydroxides Intercalated with Carbonate, Nitrate, Chloride and Sulphate Ions: Synthesis, Characterisation and Dye Removal Properties. *J. Taibah Univ. Sci.* **2017**, *11*, 90–100.
- (21) Shumaker, J. L.; Crofcheck, C.; Tackett, S. A.; Santillan-Jimenez, E.; Morgan, T.; Ji, Y.; Crocker, M.; Toops, T. J. Biodiesel Synthesis Using Calcined Layered Double Hydroxide Catalysts. *Appl. Catal. B Environ.* **2008**, *82*, 120–130.
- (22) Tathod, A. P.; Hayek, N.; Shpasser, D.; Simakov, D. S. A.; Gazit, O. M. Mediating Interaction Strength between Nickel and Zirconia Using a Mixed Oxide Nanosheets Interlayer for Methane Dry Reforming. *Appl. Catal. B Environ.* **2019**, *249*, 106–115.
- (23) Peng, F.; Wang, D.; Zhang, D.; Cao, H.; Liu, X. The Prospect of Layered Double Hydroxide as Bone Implants: A Study of Mechanical Properties, Cytocompatibility and Antibacterial Activity. *Appl. Clay Sci.* **2018**, *165*, 179–187.
- (24) Layrac, G.; Tichit, D.; Larionova, J.; Guari, Y.; Guérin, C. Controlled Growth of Cyano-Bridged Coordination Polymers into Layered Double Hydroxides. *J. Phys. Chem. C* **2011**, *115*, 3263–3271.
- (25) Lv, L.; He, J.; Wei, M.; Evans, D. G.; Zhou, Z. Treatment of High Fluoride Concentration Water by MgAl–CO<sub>3</sub> Layered Double Hydroxides: Kinetic and Equilibrium Studies. *Water Res.* **2007**, *41*, 1534–1542.
- (26) Shui, Z. H.; Yu, R.; Chen, Y. X.; Duan, P.; Ma, J. T.; Wang, X. P. Improvement of Concrete Carbonation Resistance Based on a Structure Modified Layered Double Hydroxides (LDHs): Experiments and Mechanism Analysis. *Constr. Build. Mater.* **2018**, *176*, 228–240.
- (27) Wang, H.; Chen, J.; Cai, Y.; Ji, J.; Liu, L.; Teng, H. H. Defluoridation of Drinking Water by Mg/Al Hydrotalcite-like Compounds and Their Calcined Products. *Appl. Clay Sci.* **2007**, *35*, 59–66.
- (28) Nath, J.; Dolui, S. K. Synthesis of Carboxymethyl Cellulose-g-Poly(Acrylic Acid)/LDH Hydrogel for in Vitro Controlled Release of Vitamin B12. *Appl. Clay Sci.* **2018**, *155*, 65–73.
- (29) Chen, S.; Xu, Z. P.; Zhang, Q.; Lu, G. Q. M.; Hao, Z. P.; Liu, S. Studies on Adsorption of Phenol and 4-Nitrophenol on MgAl-Mixed Oxide Derived from MgAl-Layered Double Hydroxide. *Sep. Purif. Technol.* **2009**, *67*, 194–200.
- (30) Zhang, M.; Gao, B.; Yao, Y.; Inyang, M. Phosphate Removal Ability of Biochar/MgAl-LDH Ultra-Fine Composites Prepared by Liquid-Phase Deposition. *Chemosphere* **2013**, *92*, 1042–1047.
- (31) Theiss, F. L.; Ayoko, G. A.; Frost, R. L. Iodide Removal Using LDH Technology. *Chem. Eng. J.* **2016**, *296*, 300–309.
- (32) Wang, B.; Zhang, W.; Zhang, W.; Mujumdar, A. S.; Huang, L. Progress in Drying Technology for Nanomaterials. *Dry. Technol.* **2005**, *23*, 7–32.
- (33) Wang, B. H.; Yu, C. Y.; Wang, X. Z. In *Supercritical Drying for Nanometer Porous Materials*, Proceedings of the Eighth National Drying Symposium; Harbin, 2002; pp 22–31.
- (34) Wang, Y.; Zhang, T.; Xu, S.; Wang, X.; Evans, D. G.; Duan, X. Preparation of Layered-Double Hydroxide Microspheres by Spray Drying. *Ind. Eng. Chem. Res.* **2008**, *47*, 5746–5750.
- (35) Mebrahtu, C.; Krebs, F.; Perathoner, S.; Abate, S.; Centi, G.; Palkovits, R. Hydrotalcite Based Ni–Fe/(Mg, Al)O<sub>x</sub> Catalysts for Methanation - Tailoring Fe Content for Improved CO Dissociation, Basicity, and Particle Size. *Catal. Sci. Technol.* **2018**, *8*, 1016–1027.
- (36) Mann, S.; Ozin, G. A. Synthesis of Inorganic Materials With Complex Form. *Nature* **1996**, *382*, 313–318.
- (37) Anchieta, C. G.; Assaf, E. M.; Assaf, J. M. Effect of Ionic Liquid in Ni/ZrO<sub>2</sub> Catalysts Applied to Syngas Production by Methane Tri-Reforming. *Int. J. Hydrogen Energy* **2019**, *44*, 9316–9327.
- (38) Moriyama, S.; Sasaki, K.; Hirajima, T. Effect of Freeze Drying on Characteristics of Mg–Al Layered Double Hydroxides and Bimetallic Oxide Synthesis and Implications for Fluoride Sorption. *Appl. Clay Sci.* **2016**, *132–133*, 460–467.
- (39) Julklang, W.; Wangriya, A.; Golman, B. Fabrication of Layered Double Hydroxide Microspheres by Spray Drying of Nanoparticles: Effects of Process Conditions. *Mater. Lett.* **2017**, *209*, 429–432.
- (40) Goh, K. H.; Lim, T. T.; Dong, Z. Application of Layered Double Hydroxides for Removal of Oxyanions: A Review. *Water Res.* **2008**, *42*, 1343–1368.
- (41) Legrouri, A.; Lakraimi, M.; Barroug, A.; De Roy, A.; Besse, J. P. Removal of the Herbicide 2,4-Dichlorophenoxyacetate from Water to Zinc-Aluminium-Chloride Layered Double Hydroxides. *Water Res.* **2005**, *39*, 3441–3448.
- (42) Yun, S. K.; Pinnavaia, T. J. Layered Double Hydroxides Intercalated by Polyoxometalate Anions with Keggin ( $\alpha$ -H<sub>2</sub>W<sub>12</sub>O<sub>40</sub>6-), Dawson ( $\alpha$ -P<sub>2</sub>W<sub>18</sub>O<sub>62</sub>6-), and Finke (Co<sub>4</sub>(H<sub>2</sub>O)-<sub>2</sub>(PW<sub>9</sub>O<sub>34</sub>)<sub>2</sub>10-) Structures. *Inorg. Chem.* **1996**, *35*, 6853–6860.
- (43) Radha, A. V.; Kamath, P. V.; Shivakumara, C. Conservation of Order, Disorder, and “Crystallinity” during Anion-Exchange Reactions among Layered Double Hydroxides (LDHs) of Zn with Al. *J. Phys. Chem. B* **2007**, *111*, 3411–3418.
- (44) Motevalizadeh, L.; Heidary, Z.; Abrishami, M. E. Facile Template-Free Hydrothermal Synthesis and Microstrain Measurement of ZnO Nanorods. *Bull. Mater. Sci.* **2014**, *37*, 397–405.
- (45) Kibasomba, P. M.; Dhlamini, S.; Maaza, M.; Liu, C. P.; Rashad, M. M.; Rayan, D. A.; Mwakikunga, B. W. Strain and Grain Size of TiO<sub>2</sub> Nanoparticles from TEM, Raman Spectroscopy and XRD: The Revisiting of the Williamson-Hall Plot Method. *Results Phys.* **2018**, *9*, 628–635.
- (46) Thommes, M.; Kaneko, K.; Neimark, A. V.; Olivier, J. P.; Rodriguez-Reinoso, F.; Rouquerol, J.; Sing, K. S. W. Physisorption of Gases, with Special Reference to the Evaluation of Surface Area and Pore Size Distribution (IUPAC Technical Report). *Pure Appl. Chem.* **2015**, *87*, 1051–1069.
- (47) Rives, V.; Kannan, S. Layered Double Hydroxides with the Hydrotalcite-Type Structure Containing Cu<sup>2+</sup>, Ni<sup>2+</sup> and Al<sup>3+</sup>. *J. Mater. Chem.* **2000**, *10*, 489–495.
- (48) Xue, L.; Gao, B.; Wan, Y.; Fang, J.; Wang, S.; Li, Y.; Muñoz-Carpena, R.; Yang, L. High Efficiency and Selectivity of MgFe-LDH Modified Wheat-Straw Biochar in the Removal of Nitrate from Aqueous Solutions. *J. Taiwan Inst. Chem. Eng.* **2016**, *63*, 312–317.
- (49) Santos, R. M. M.; dos Gonçalves, R. G. L.; Constantino, V. R. L.; Santilli, C. V.; Borges, P. D.; Tronto, J.; Pinto, F. G. Adsorption of Acid Yellow 42 Dye on Calcined Layered Double Hydroxide: Effect of Time, Concentration, PH and Temperature. *Appl. Clay Sci.* **2017**, *140*, 132–139.
- (50) Barsoum, M. *Fundamentals of Ceramics*, 1st ed.; CRC Press, 2002.
- (51) Pérez-Ramírez, J.; Mul, G.; Kapteijn, F.; Moulijn, J. A. A Spectroscopic Study of the Effect of the Trivalent Cation on the Thermal Decomposition Behaviour of Co-Based Hydrotalcites. *J. Mater. Chem.* **2001**, *11*, 2529–2536.
- (52) Stevens, R. W., Jr; Siriwardane, R. V.; Logan, J. In Situ Fourier Transform Infrared (FTIR) Investigation of CO<sub>2</sub> Adsorption onto Zeolite Materials. *Energy Fuels* **2008**, *22*, 3070–3079.
- (53) Mourid, E. H.; Lakraimi, M.; Lhaj, B.; Elkhatabi, E. H.; Legrouri, A. Wastewater Treatment Test by Removal of the Sulfamethoxazole Antibiotic by a Calcined Layered Double Hydroxide. *Appl. Clay Sci.* **2019**, *168*, 87–95.
- (54) Bolognini, M.; Cavani, F.; Scagliarini, D.; Flego, C.; Perego, C.; Saba, M. Heterogeneous Basic Catalysts as Alternatives to Homogeneous Catalysts: Reactivity of Mg/Al Mixed Oxides in the Alkylation of m-Cresol with Methanol. *Catal. Today* **2002**, *75*, 103–111.
- (55) León, M.; Díaz, E.; Bennici, S.; Vega, A.; Ordóñez, S.; Auroux, A. Adsorption of CO<sub>2</sub> on Hydrotalcite-Derived Mixed Oxides: Sorption Mechanisms and Consequences for Adsorption Irreversibility. *Ind. Eng. Chem. Res.* **2010**, *49*, 3663–3671.
- (56) Palmer, S. J.; Nguyen, T.; Frost, R. L. Synthesis and Raman Spectroscopic Characterisation of Hydrotalcite with CO<sub>3</sub><sup>2-</sup> and VO<sub>3</sub><sup>-</sup> Anions in the Interlayer. *J. Raman Spectrosc.* **2007**, *38*, 1602–1608.
- (57) Rajak, U.; Nashine, P.; Verma, T. N. Effect of Spirulina Microalgae Biodiesel Enriched with Diesel Fuel on Performance and Emission Characteristics of CI Engine. *Fuel* **2020**, *268*, No. 117305.

- (58) Rege, S. U.; Yang, R. T. A Novel FTIR Method for Studying Mixed Gas Adsorption at Low Concentrations: H<sub>2</sub>O and CO<sub>2</sub> on NaX Zeolite and  $\gamma$ -Alumina. *Chem. Eng. Sci.* **2001**, *56*, 3781–3796.
- (59) Kouva, S.; Andersin, J.; Honkala, K.; Lehtonen, J.; Lefferts, L.; Kanervo, J. Water and Carbon Oxides on Monoclinic Zirconia: Experimental and Computational Insights. *Phys. Chem. Chem. Phys.* **2014**, *16*, 20650–20664.
- (60) Kouva, S.; Honkala, K.; Lefferts, L.; Kanervo, J. Review: Monoclinic Zirconia, Its Surface Sites and Their Interaction with Carbon Monoxide. *Catal. Sci. Technol.* **2015**, *5*, 3473–3490.
- (61) Markov, L.; Blaskov, V.; Klissurski, D.; Nikolov, S. The Thermal Decomposition Mechanism of Iron(III) Hydroxide Carbonate to  $\alpha$ -Fe<sub>2</sub>O<sub>3</sub>. *J. Mater. Sci.* **1990**, *25*, 3096–3100.
- (62) Lv, L.; He, J.; Wei, M.; Evans, D. G.; Duan, X. Uptake of Chloride Ion from Aqueous Solution by Calcined Layered Double Hydroxides: Equilibrium and Kinetic Studies. *Water Res.* **2006**, *40*, 735–743.
- (63) Rives, V. Study of Layered Double Hydroxides by Thermal Methods. In *Layered Double Hydroxides: Present and Future*, Rives, V., Ed.; Nova Science Publishers: Nova York, 2001; pp 127–152.
- (64) Miyata, S. Physico-Chemical Properties of Synthetic Hydroxycates in Relation to Composition. *Clays Clay Miner.* **1980**, *28*, 50–56.
- (65) Yun, S. K.; Pinnavaia, T. J. Layered Double Hydroxides Intercalated by Polyoxometalate Anions with Keggin ( $\alpha$ -H<sub>2</sub>W<sub>12</sub>O<sub>40</sub>6-), Dawson ( $\alpha$ -P<sub>2</sub>W<sub>18</sub>O<sub>62</sub>6-), and Finke (Co<sub>4</sub>(H<sub>2</sub>O)-<sub>2</sub>(PW<sub>9</sub>O<sub>34</sub>)<sub>2</sub>10-) Structures. *Inorg. Chem.* **1996**, *35*, 6853–6860.
- (66) Stanimirova, T.; Piperov, N.; Petrova, N.; Kirov, G. Thermal Evolution of Mg-Al-CO<sub>3</sub> Hydroxycates. *Clay Miner.* **2004**, *39*, 177–191.
- (67) Braterman, P. S.; Xu, Z. P.; Yarberr, F. Layered Double Hydroxides (LDHs). In *Handbook of Layered Materials*, Auerbach, S. M.; Carrado, K. A.; Dutta, P. K., Eds.; CRC Press: Nova York, 2004; Vol. 1, p 664.
- (68) Yang, W.; Kim, Y.; Liu, P. K. T.; Sahimi, M.; Tsotsis, T. T. A Study by in Situ Techniques of the Thermal Evolution of the Structure of a Mg-Al-CO<sub>3</sub> Layered Double Hydroxide. *Chem. Eng. Sci.* **2002**, *57*, 2945–2953.
- (69) Rey, F.; Fornés, V.; Rojo, J. M. Thermal Decomposition of Hydroxycates. An Infrared and Nuclear Magnetic Resonance Spectroscopic Study. *J. Chem. Soc. Faraday Trans.* **1992**, *88*, 2233–2238.
- (70) Lee, S. Y.; Choi, J. W.; Song, K. G.; Choi, K.; Lee, Y. J.; Jung, K. W. Adsorption and Mechanistic Study for Phosphate Removal by Rice Husk-Derived Biochar Functionalized with Mg/Al-Calcined Layered Double Hydroxides via Co-Pyrolysis. *Compos. Part B: Eng.* **2019**, *176*, No. 107209.
- (71) Stanimirova, T.; Vergilov, I.; Kirov, G.; Petrova, N. Thermal Decomposition Products of Hydroxycate-like Compounds: Low-Temperature Metaphases. *J. Mater. Sci.* **1999**, *34*, 4153–4161.
- (72) Miyata, S.; Okada, A. Synthesis of Hydroxycate-Like Compounds and Their Physico-Chemical Properties—The Systems Mg<sub>2</sub>+Al<sub>3</sub>+SO<sub>4</sub><sup>2-</sup> and Mg<sub>2</sub>+Al<sub>3</sub>+CrO<sub>4</sub><sup>2-</sup>. *Clays Clay Miner.* **1977**, *25*, 14–18.
- (73) Stanimirova, T.; Hibino, T.; Balek, V. Thermal Behavior of Mg-Al-CO<sub>3</sub> Layered Double Hydroxide Characterized by Emanation Thermal Analysis. *J. Therm. Anal. Calorim.* **2006**, *84*, 473–478.
- (74) Han, S.; Hou, W.; Zhang, C.; Sun, D.; Huang, X.; Wang, G. Structure and the Point of Zero Charge of Magnesium Aluminum of Hydroxide. *J. Chem. Soc., Faraday Trans.* **1998**, *94*, 915–918.
- (75) Zhao, Y.; Li, F.; Zhang, R.; Evans, D. G.; Duan, X. Preparation of Layered Double-Hydroxide Nanomaterials with a Uniform Crystallite Size Using a New Method Involving Separate Nucleation and Aging Steps. *Chem. Mater.* **2002**, *14*, 4286–4291.
- (76) Reichle, W. T. Synthesis of Anionic Clay Minerals (Mixed Metal Hydroxides, Hydroxycate). *Solid States Ionics* **1986**, *22*, 135–141.
- (77) Gonçalves, N. S.; Carvalho, J. A.; Lima, Z. M.; Sasaki, J. M. Size-Strain Study of NiO Nanoparticles by X-Ray Powder Diffraction Line Broadening. *Mater. Lett.* **2012**, *72*, 36–38.
- (78) Brito, A.; Borges, M. E.; Garín, M.; Hernández, A. Biodiesel Production from Waste Oil Using Mg-Al Layered Double Hydroxide Catalysts. *Energy Fuels* **2009**, *23*, 2952–2958.
- (79) Pagano, C.; Marmottini, F.; Nocchetti, M.; Ramella, D.; Perioli, L. Effects of Different Milling Techniques on the Layered Double Hydroxides Final Properties. *Appl. Clay Sci.* **2018**, *151*, 124–133.